Atmospheric odd nitrogen response to electron forcing from a 6D magnetospheric hybrid-kinetic simulation

Tuomas Häkkilä[1], Maxime Grandin[2], Markus Battarbee[2], Monika E. Szeląg[1], Markku Alho[2], Leo Kotipalo[2], Niilo Kalakoski[1], Pekka T. Verronen[1,3], and Minna Palmroth[1,2]

[1]Space and Earth Observation Centre, Finnish Meteorological Institute, Helsinki, Finland
[2]Department of Physics, University of Helsinki, Helsinki, Finland
[3]Sodankylä Geophysical Observatory, University of Oulu, Sodankylä, Finland

Correspondence: Tuomas Häkkilä (tuomas.hakkila@fmi.fi)

Abstract. Modelling the distribution of odd nitrogen (NO_x) in the polar middle and upper atmosphere has proven to be a complex task. Firstly, its production by energetic electron precipitation is highly variable on hourly time scales. Secondly, there are uncertainties in the measurement-based but simplified electron flux data sets that are currently used in atmosphere and climate models. The altitude distribution of NO_x is strongly affected by atmospheric dynamics also on monthly time

5   scales, particularly in the polar winter periods when the isolated air inside the polar vortex descends from lower thermosphere to mesosphere and stratosphere. Recent comparisons between measurements and simulations have revealed strong differences in the NO_x distribution, with questions remaining about the representation of both production and transport in models. Here we present for the first time a novel approach, where the electron atmospheric forcing in the auroral energy range (50 eV – 50 keV) is derived from a magnetospheric hybrid-kinetic simulation with a detailed description of energy range and resolution,

10   and spatial and diurnal distribution. These electron data are used as input in a global whole atmosphere model to study the impact on polar NO_x and ozone. We will show that the magnetospheric electron data provides a realistic representation of the forcing which leads to considerable impact in the lower thermosphere, mesosphere and stratosphere. We find that during the polar winter the simulated auroral electron precipitation increases the polar NO_x concentrations up to 200 %, 50 %, and 7 % in the lower thermosphere, mesosphere, and upper stratosphere, respectively, when compared to no auroral electron forcing in

15   the atmospheric model. These results demonstrate the potential of combining magnetospheric and atmospheric simulations for detailed studies of solar wind – atmosphere coupling.

1 Introduction

Understanding the polar mesosphere–lower thermosphere–ionosphere (MLTI) region presents a unique challenge. The MLTI

20   covers the approximate altitude range 80–200 km, and is hence simultaneously too high for many ground-based observations and too low for efficient in-situ satellite-borne measurements (Palmroth et al., 2021). Therefore accurate modelling of the

MLTI is required to complement the scarce direct measurements to further our knowledge of the region. The polar MLTI (polewards of $60°$) depends on solar radiation, which drives both diurnal and seasonal effects due to the planet's rotation and axis of inclination. The magnetosphere, with its many poorly understood mechanisms, also controls the physical state

25 of the polar MLTI through its electromagnetic forcing (e.g. Sarris et al., 2023). Hence the polar MLTI is characterized by complex dynamics between the neutral atmosphere and the electromagnetic ionosphere, leading to great uncertainties in our understanding of the region.

Nitric Oxide (NO), a member of the odd nitrogen family (NO_x, defined as the sum of N, NO, and NO_2), is one of the most important species in the polar MLTI energetics (e.g. Mlynczak et al., 2005). NO_x is produced in the atmosphere as the

30 result of solar energetic radiation while in the polar regions energetic particle precipitation (EPP) also becomes a major source (Barth et al., 2001). Through its descent inside the polar vortex, NO_x also provides a dynamical connection between MLTI and stratospheric altitudes (Funke et al., 2014). In the upper stratosphere, NO_x transport from above leads to depletion of ozone which can be measured using satellite-based instruments (Damiani et al., 2016). Because ozone strongly absorbs solar ultraviolet radiation, it is one of the main constituents determining the thermal structure of the stratosphere. Through ozone,

35 NO_x can have an impact on the radiative balance of the polar atmosphere beyond just within the MLTI.

There are essentially three EPP sources of NO_x: solar protons, radiation belt electrons, and auroral electrons (Verronen and Rodger, 2015). The energy of solar protons and radiation belt electrons are large enough for them to penetrate and produce NO_x in the mesosphere and stratosphere, allowing a more direct impact on ozone. These two sources of NO_x can currently be represented in long-term atmospheric and climate simulations although uncertainties are still present in the latter (Matthes

40 et al., 2017; Sinnhuber et al., 2021). Because the precipitation of auroral electrons, the third source of NO_x, is restricted to thermospheric altitudes due to its lower energy, its impact on the stratospheric ozone balance is to a larger extent affected by polar atmosphere dynamics and is not fully understood. Auroral electrons originate in the magnetosphere, chiefly via substorms, where the magnetotail suddenly disrupts and launches a vast number of electrons and protons of variable energies towards the ionosphere (Palmroth et al., 2017; Palmroth et al., 2023). Substorms and pulsating aurora, a phenomenon during the substorm

45 recovery phase, have been shown to produce NO_x (Seppälä et al., 2015; Turunen et al., 2016). As substorms occur on a regular basis, the forcing from auroral electron precipitation also takes place on a roughly daily basis (Partamies et al., 2013). In long-term climate simulations, models typically include the NO_x production from auroral electrons using proxy models based on geomagnetic indices, and typically use a simplistic representation for their energy spectrum (e.g. Marsh et al., 2007).

Atmospheric models are struggling to produce correct amounts of NO_x in the MLTI when compared to observations (Randall

50 et al., 2015). This inaccuracy leads to an incomplete representation of the radiative balance within the polar region through the NO_x impact on stratospheric ozone (Szeląg et al., 2022). The suggested reasons for NO_x deficit include underestimation of radiation belt electron forcing (Hendrickx et al., 2018). However, the production from auroral electrons ($<30\,keV$) likely also plays a role in the discrepancy because it is a relatively continuous as well as probably the largest contributor to the overall NO_x budget in the polar MLTI (Sinnhuber et al., 2011). The simplified inclusion of auroral electrons in atmospheric

55 simulations is incomplete both in terms of auroral electron fluxes and spectra, and these may account for the missing NO_x production. Further, the transport of thermospheric NO_x to the mesosphere and lower altitudes remains a challenge in models

(Meraner and Schmidt, 2016; Smith-Johnsen et al., 2022) The lack of detailed, long-term auroral electron forcing in climate models could therefore obstruct accurate evaluation of polar climate variability.

In this paper, we report on the first-time combination of magnetospheric and atmospheric modelling, with the aim of quantifying the auroral electron impact on NO_x and ozone. We use eVlasiator, a variant of the global hybrid-Vlasov model Vlasiator, to simulate the electron fluxes at auroral energies from $50\,eV$ to $50\,keV$. Compared to proxy-based parameterizations, the modelled magnetospheric electron fluxes characterise the altitude extent and distribution of the forcing in more detail. Atmospheric ionization rates derived from these fluxes are then used in the Whole Atmosphere Community Climate Model (WACCM) to determine auroral electron impact on NO_x and ozone from the MLTI to the upper stratosphere. Finally, we discuss the potential of the magnetosphere-atmosphere coupling in understanding the solar wind – atmosphere coupling and outline future steps of development.

2 Methods

2.1 Vlasiator and eVlasiator

Vlasiator is a global hybrid-Vlasov model simulating ion-kinetic plasma physics of near-Earth space (Palmroth et al., 2018), which recently became capable of running 6D simulations (Ganse et al., 2023). Vlasiator models the collisionless ion populations directly as velocity distribution functions (VDFs), discretized on Cartesian grids, allowing for accurate representation of phenomena such as wave-particle interactions (Dubart et al., 2020) and precipitating protons (Grandin et al., 2019, 2020, 2023), which cannot be modelled using the magnetohydrodynamic (MHD) codes (Palmroth et al., 2006). The spatial simulation domain is divided into either a uniform Cartesian 2D spatial mesh or a Cartesian 3D mesh with regions of interest refined with an octree cell-based refinement algorithm (Ganse et al., 2023; Kotipalo et al., 2024). Each spatial cell contains a 3D velocity mesh consisting of cubic uniform Cartesian cells. In order to fit the massive amount of simulation data into memory, Vlasiator utilizes a sparse algorithm (von Alfthan et al., 2014) where only those regions of velocity space which are deemed to contribute to plasma moments in a significant fashion are stored and propagated. This is implemented through discarding blocks of the grid which have phase-space density below a pre-defined threshold, yet maintaining a buffer region around those cells in order to ensure physical behaviour at the edges of the velocity domain. The simulation state is propagated directly via the Vlasov equation, with fields solved on a regular Cartesian grid and closure provided by MHD Ohm's law with the Hall and electron pressure gradient terms included.

A typical Vlasiator simulation models the global geomagnetic domain of the Earth, spanning tens to hundreds of Earth radii ($R_E = 6371\,km$) in each dimension with a spatial resolution of the order of the ion inertial length, and with an inner boundary positioned at roughly 5 Earth radii. The velocity grid is defined so to be able to discretize the inflowing solar wind. The Earth's magnetic field is modeled at full strength, facilitating direct comparison with spacecraft observations. Sample simulation parametrizations can be found for example in Horaites et al. (2023) and Palmroth et al. (2023). Vlasiator runs are propagated on the order of hundreds to thousands of seconds, in order to facilitate self-consistent formation of the magnetospheric domain and its dynamics, but constrained by the availability of computational resources.

eVlasiator is an offshoot of Vlasiator which considers electrons as a kinetic population (Battarbee et al., 2021) instead of the usual ions. eVlasiator is not a standard full-kinetic plasma code, instead evaluting electron response to ion-scale structures and fields. What eVlasiator does provide is realistic electron VDFs evaluated for a single point in time from a larger Vlasiator simulation, such as presented in Alho et al. (2022) and validated against spacecraft observations. Since Alho et al. (2022), eVlasiator has been extended to work on 6D Vlasiator inputs, with the code available via Zenodo (Pfau-Kempf et al., 2022). Thus, eVlasiator can be used to infer kinetic electron VDFs along connected field lines, and thus also allowing the calculation of precipitating electron fluxes. Due to numerical constraints, eVlasiator utilizes a reduced mass ratio, for example $m_p/m_e \approx$ 183.6 in Alho et al. (2022).

2.2 Simulating precipitating particle fluxes

In (e)Vlasiator, precipitating particle differential number fluxes are calculated in every ordinary space cell, at every output time step in the simulation. At a given position $\mathbf{r}$ in ordinary space, the precipitating electron differential number flux value at energy E is given by

$$\mathcal{F}_e(E, \mathbf{r}) = \frac{v^2}{m_e} \langle f_e(\mathbf{r}, v, \theta, \varphi) \rangle_{\theta_0} \tag{1}$$

with $v = \sqrt{2E/m_e}$ the corresponding electron speed, m_e the electron mass, f_e the electron phase-space density, θ the pitch angle, φ the gyrophase angle, and θ_0 the bounce loss cone angle, and where $\langle . \rangle_{\theta_0}$ denotes averaging inside the loss cone. The full derivation of the version of Eq. (1) for proton fluxes can be found in Grandin et al. (2019). Subsequent studies investigating dayside and nightside auroral proton precipitation under various driving conditions are presented in Grandin et al. (2020, 2023) and Horaites et al. (2023).

In this study, we present for the first time precipitating electron fluxes obtained with eVlasiator. The Vlasiator run used as the basis for the eVlasiator simulation is the same as described in e.g. Palmroth et al. (2023), and the eVlasiator run is the first 3D-3V magnetospheric eVlasiator simulation. The Vlasiator simulation is driven by a solar wind of $V_x = -750\,\mathrm{km\,s^{-1}}$ with a density of $n_\mathrm{p} = 10^6\,\mathrm{m^{-3}}$ and a temperature of $0.5\,\mathrm{MK}$. The inner boundary consists of stationary plasma at a radius of $4.7\,R_\mathrm{E}$ and is modelled as a near-conducting sphere. The spatial mesh has a base resolution of $8000\,\mathrm{km}$ at the lowest refinement level, increasing up to $1000\,\mathrm{km}$ in regions of interest such as the magnetotail and the magnetopause. The ion velocity cell resolution is $40\,\mathrm{km\,s^1}$. The Vlasiator simulation was propagated for a total of 1506 seconds. The eVlasiator run based on the final state of the magnetospheric Vlasiator simulation utilized a mass ratio of $m_p/m_e = 40$ and an electron velocity cell resolution of $128\,\mathrm{km\,s^{-1}}$, whilst maintaining the spatial resolution and fields of the Vlasiator simulation. Due to computational constraints, the eVlasiator simulation was run selectively on the inner magnetosphere only, spanning $X \in [-20.1, 17.6]\,R_\mathrm{E}$ and $Y, Z \in [-20.1, +20.1]\,R_\mathrm{E}$, and was propagated for a time extent of $1.4\,\mathrm{s}$. Figure 1 shows the Vlasiator and eVlasiator simulation domains and examples of electron velocity distributions in eVlasiator.
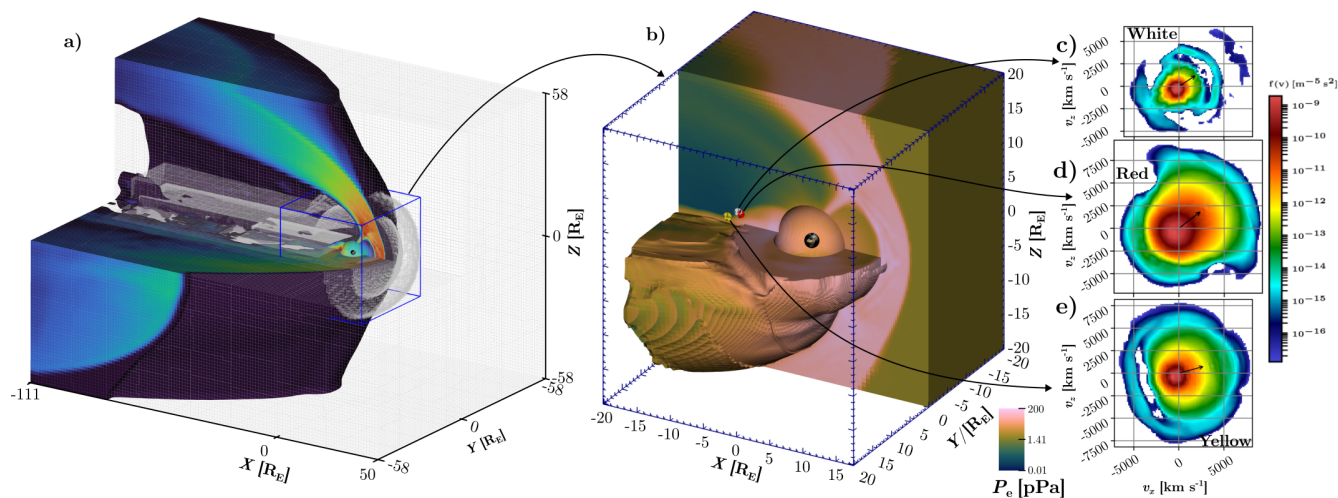
Figure 1. (a) Vlasiator simulation of the 3D-3V magnetospheric simulation, grid refinement regions (gray grids) and the interior of the magnetosphere, with the extracted eVlasiator domain shown as a blue box. (b) Overview of the eVlasiator simulation at its final state, with electron pressure shown on the bow shock, magnetopause, and the southern lobe. Earth is visible inside the spherical inner boundary of the simulation domain. (c–e) Sample electron VDFs from eVlasiator on the midnight meridian, from the white, red, and yellow markers in panel b, showing field-aligned beams.

2.3 Construction of the auroral-electron forcing dataset

2.3.1 Mapping of the ionosphere grid to the eVlasiator simulation domain

To obtain the forcing dataset for WACCM consisting of precipitating electron fluxes at auroral energies (0.05–50 keV) as a function of magnetic local time (MLT) and geomagnetic latitude (MLAT), we first construct a MLT–MLAT grid at ionospheric altitudes, which we map to the magnetosphere. The procedure is similar to that presented in Grandin et al. (2023), with a notable difference to account for the specific setup of the eVlasiator run. It is described in detail in Appendix A.

It is worth highlighting that the obtained precipitating electron fluxes are the result of the physical processes described in the eVlasiator simulation. These do not include some of the important processes for auroral electron acceleration and pitch-angle scattering, such as inner-magnetospheric waves or field-aligned potential drops above the ionosphere. As a consequence, the precipitating fluxes extracted from the eVlasiator run are lower than in reality. For this reason, calibration with observational data has been performed as explained in the next section.

2.3.2 Calibration of the eVlasiator fluxes with DMSP observations

To calibrate the eVlasiator differential number fluxes with observations, we use two pairs of overpasses of Defense Meteorological Satellite Program (DMSP) spacecraft during similar driving conditions. Each pair contains a polar cusp overpass in the northern hemisphere (NH) and a nightside oval overpass in the southern hemisphere (SH). The dates of the events are 1 August 2011 (06:00–07:30 UT) and 10 October 2015 (05:30–06:30 UT). We use measurements from the Special Sensor J (SSJ) instrument (Redmon et al., 2017), which provides particle counts within a field of view spanning $4° \times 90°$ in the observation plane (Hardy et al., 2008). Precipitating electron differential number fluxes are collected in 19 logarithmically spaced energy bins between $30\,\mathrm{eV}$ and $30\,\mathrm{keV}$. For the first (second) event, SSJ measurements from the DMSP-F16 (F17) and DMSP-F18 (F17) spacecraft are considered. These two events were previously used for precipitating proton flux comparison between Vlasiator and observations in Grandin et al. (2023).

A detailed description of the eVlasiator flux calibration based on the DMSP observations is given in Appendix B. In summary, we apply an energy-dependent correction factor to the eVlasiator fluxes in the polar cusp and in the nightside auroral oval. There is one such correcting function for the cusp fluxes, $\alpha_{\mathrm{day}}(E)$, and another one for the nightside fluxes, $\alpha_{\mathrm{night}}(E)$. We first calculate the ratio between the measured differential number fluxes by DMSP/SSJ and those obtained with eVlasiator, along the DMSP orbit, separately for the dayside and nightside overpasses. Then, for a given electron energy, we examine the distribution of the obtained ratios, and retain a certain quantile for which we fit a polynomial function (as a function of energy). Which quantile we retain is determined such that the ratio between the integrated energy fluxes is close to one (see Appendix B4 for details). We have determined that the 61st (67th) quantile optimally fulfils this condition for the dayside (nightside) ratios.

2.4 Whole Atmosphere Community Climate Model

The Whole Atmosphere Community Climate Model (WACCM) is a global 3-D chemistry-climate model that covers the altitude range from the surface up to about $140\,\mathrm{km}$. The model incorporates various physical processes and interactions within the atmosphere, including dynamics, chemistry, radiation, and their interactions with the Earth's surface and external forcings such as solar radiation and greenhouse gases (Marsh et al., 2013; Gettelman et al., 2019). Here, we use WACCM-D, a variant of WACCM that enhances standard parameterizations of HO_x and NO_x production by incorporating a comprehensive ionospheric chemistry. This alteration aims to better replicate the observed impacts of energetic particle precipitation on the composition of the mesosphere and upper stratosphere (Verronen et al., 2016; Andersson et al., 2016). We conducted specified dynamics simulations (SD) where horizontal winds, temperature, pressure, surface stress and heat fluxes are adjusted to 3 hourly Modern-Era Retrospective Analysis for Research and Applications (MERRA-2) reanalysis data (Molod et al., 2015). The model is constrained by the reanalysis data up to about $50\,\mathrm{km}$ while the dynamics are free-running at altitudes above. We use version 6 of the model with a latitude $\times$ longitude resolution of $0.95° \times 1.25°$.

As a default, WACCM input of solar and geomagnetic forcing is taken as recommended for the Coupled Model Intercomparison Project Phase 6 (Matthes et al., 2017). In addition to total and spectral irradiance, this data set also includes atmospheric

ionization rates due to solar protons, medium-energy electrons, and galactic cosmic rays. The auroral electron precipitation,
however, is driven by the geomagnetic Kp index, and represented by a Maxwellian energy distribution and a characteristic
energy of $2\,\mathrm{keV}$ (Roble and Ridley, 1987). Further, to account for the impact of electron forcing above its altitude range,
WACCM makes use of the three-dimensional nitric oxide empirical model (NOEM) to set NO at the model upper boundary.
NOEM is driven by Kp, day of year, and solar $10.7\,\mathrm{cm}$ radio flux (Marsh et al., 2004).

2.4.1 Atmospheric ionization rates

Using the eVlasiator electron energy–flux spectra, we calculated corresponding forcing for our WACCM atmospheric simula-
tions. In WACCM-D, ionization by EPP drives the initial production rates of ions and neutrals due to particle impact ionization,
dissociative ionization, and secondary electron dissociation (Verronen et al., 2016, Table 1). These rates are incorporated in the
WACCM ion and neutral chemistry scheme, connecting EPP forcing to the NO_x and ozone concentrations.

The atmospheric ionization rates were calculated at magnetic latitudes between $63°$ and $88°$ in both hemispheres with one
degree spacing. A half-an-hour temporal resolution was used for the magnetic local time throughout the day. Electron energy
range from $50\,\mathrm{eV}$ to $50\,\mathrm{keV}$ was considered with 32 individual grid points. We made use of the method of parameterized
electron impact ionization by Fang et al. (2010). Atmosphere for the calculation was calculated using the NRLMSIS-00 model
by Picone et al. (2002). This is the same method that was used to create electron ionization rates for the Coupled Model
Intercomparison Project Phase 6 (van de Kamp et al., 2016; Matthes et al., 2017). Here, however, the electron flux data
are not from a proxy model based on satellite observations but from the eVlasiator magnetospheric simulations. Figure 2
shows an example of eVlasiator spectra and corresponding atmospheric ionization rates. Large differences in fluxes at different
geomagnetic latitudes result in a similarly large range of ionization. According to the spectral energy range (electron energies
$<50\,\mathrm{keV}$), the bulk ionization is restricted to altitudes above $90\,\mathrm{km}$.

2.4.2 WACCM simulation setup and output

All WACCM simulations were set up using the recommended CMIP6 solar and geomagnetic forcing (Matthes et al., 2017).
WACCM-D was run from January 2005 to June 2006 in order to cover both southern and northern hemispheric winters. In this
study, we consider daily average outputs of the ionization rates, as well as NO_x and ozone concentrations.

In order to better implement the eVlasiator derived ionization rates, we input the forcing on a magnetic local time dependent
grid. For this purpose, we created a modification for WACCM, which enables MLAT $\times$ MLT ionization forcing and turns off
the Kp index driven parameterized aurora, in order to fully replace WACCM's default aurora with eVlasiator (Häkkilä, 2024).
In addition to geomagnetic latitude, support for L-shell $\times$ MLT grids is also included, as well as a version that does not turn
off the Kp aurora. The MLT-dependency code requires daily forcing files, but supports multiple time steps per daily file.

Two WACCM-D simulations were performed using the MLT-dependent ionization input. First, a simulation with the eVlasiator-
derived ionization rates as input in WACCM-D on a MLAT $\times$ MLT grid of $1° \times 0.5\,\mathrm{h}$ resolution (VLAS). For each day of the
simulation we use the same ionization data, since only one time step was available from the eVlasiator output. The second
MLT-dependent run was a reference simulation, with the ionization from auroral electrons set to 0 at all gridpoints. This way
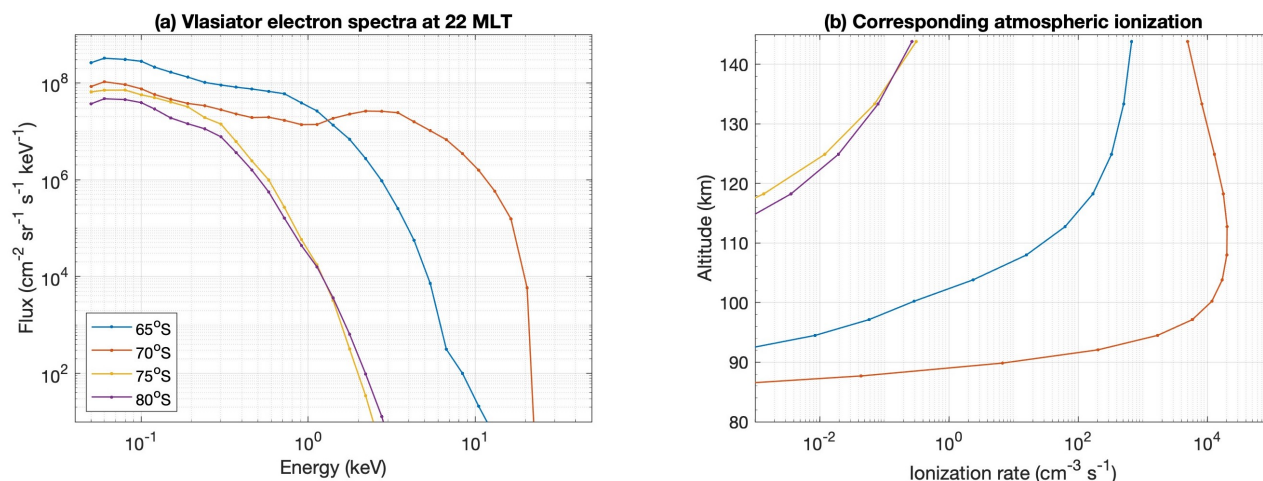
Figure 2. (a) eVlasiator electron spectra at 22 hours of magnetic local time at four Southern Hemisphere magnetic latitudes. (b) Corresponding atmospheric ionization rates.

the REF run has no auroral input and no Kp-driven parameterized aurora. We also performed simulations using WACCM's parameterized Kp-driven aurora, to use as comparisons against the eVlasiator auroral forcing. Since the VLAS run was performed using the same data every day, we use a fixed Kp value for the comparison runs. We performed 6 separate WACCM-D

200 runs, each with a different, fixed Kp index value from 0 to 5 (KP0–KP5), but we present here only the runs KP1 and KP2, since those most closely correspond to the level of ionization found in the eVlasiator aurora, as well as the KP0 and KP5 runs in order to give a range of the Kp-driven aurora. To ensure comparability, the Kp indices were also fixed for the MLT-dependent simulations, as Kp affects the background levels of NO_x in the model through NOEM. The Kp value was fixed to 0 for the REF run to create minimal conditions for comparisons. For VLAS, we considered the DMSP overpasses used for the

205 calibration of the eVlasiator electron fluxes, which took place during Kp index values around 2 and 3, for 1 August 2011 and 10 October 2015, respectively. We used the fixed the Kp index 2 for the VLAS run. All the WACCM-D simulations presented here and their differences are given in Table 1.

Table 1. The WACCM-D simulation runs and differences in their setups.

simulation	description	aurora	Kp index (fixed)
REF	Reference run with no aurora	none	0
KP0	Default WACCM-D run with fixed $Kp = 0$	parameterized	0
KP1	Default WACCM-D run with fixed $Kp = 1$	parameterized	1
VLAS	**Main run with eVlasiator aurora**	**eVlasiator**	**2**
KP2	Default WACCM-D run with fixed $Kp = 2$	parameterized	2
KP5	Default WACCM-D run with fixed $Kp = 5$	parameterized	5
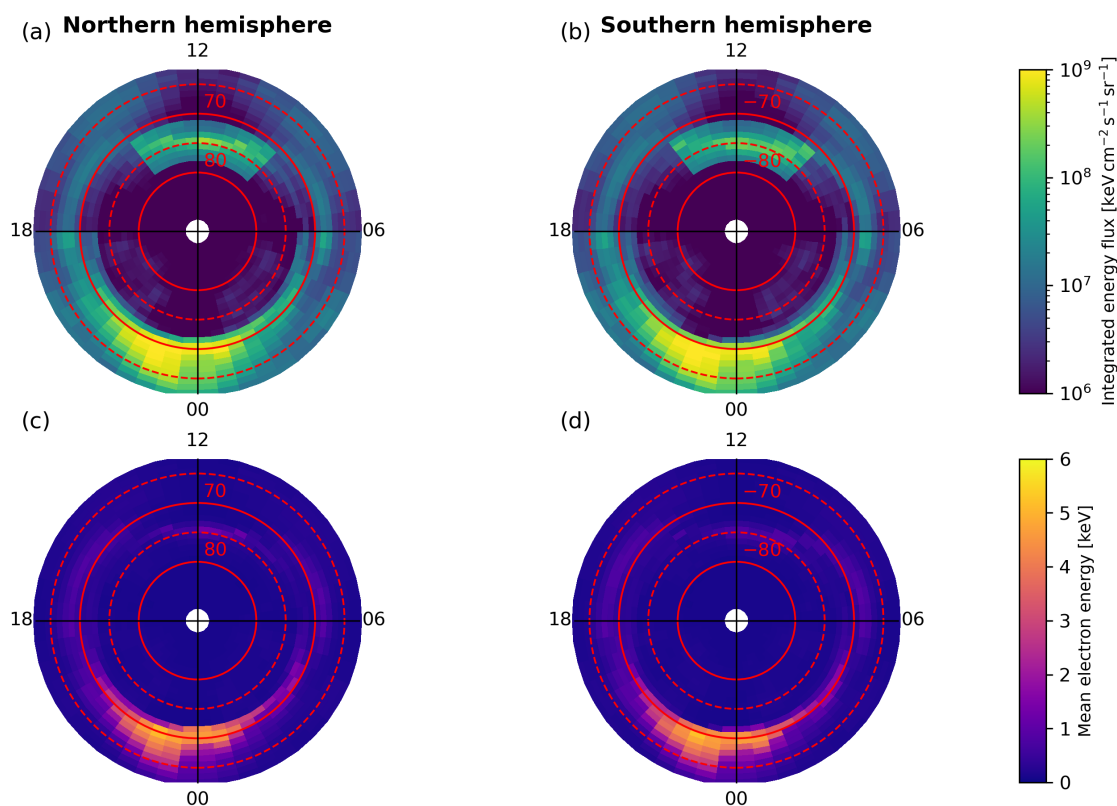
Figure 3. Polar view of integrated parameters of auroral electron precipitation in the eVlasiator run, after calibration with DMSP/SSJ observations (see Sect. 2.3.2). (a–b) Precipitating electron integrated energy flux in the northern and southern hemispheres. (c–d) Mean precipitating electron energy in the northern and southern hemisphere. In each panel, the radial coordinate is geomagnetic latitude, and the angular coordinate is magnetic local time.

3 Results

3.1 Auroral electron precipitation

3.1.1 Auroral electron fluxes from eVlasiator

Figure 3 shows the integrated parameters of the auroral electron precipitation forcing dataset obtained from eVlasiator, after the calibration with DMSP/SSJ observations (see Sect. 2.3.2). Each panel gives the data as a function of geomagnetic latitude (radial coordinate) and MLT (angular coordinate). Figures 3a and 3b show the precipitating electron integrated energy flux in the

northern and southern hemispheres, respectively. We can identify the cusp region on the dayside, between $70°$ and $80°$ MLAT

215 and within 9–15 MLT, with flux magnitudes on the order of $10^8\,\mathrm{keV\,cm^{-2}\,s^{-1}\,sr^{-1}}$. On the nightside, the integrated energy flux peaks in the pre-midnight sector and within 65–70° MLAT, reaching magnitudes on the order of $10^9\,\mathrm{keV\,cm^{-2}\,s^{-1}\,sr^{-1}}$. The forcing is very symmetrical on the nightside, whereas slight differences can be noted in the polar cusps – these results are similar to those obtained for auroral proton precipitation and discussed in Grandin et al. (2023). Figures 3c and 3d present the mean precipitating electron energy. Values are below $1\,\mathrm{keV}$ on the dayside and reach up to $5\,\mathrm{keV}$ on the nightside.

220 ### 3.1.2 Ionisation rates from WACCM-D
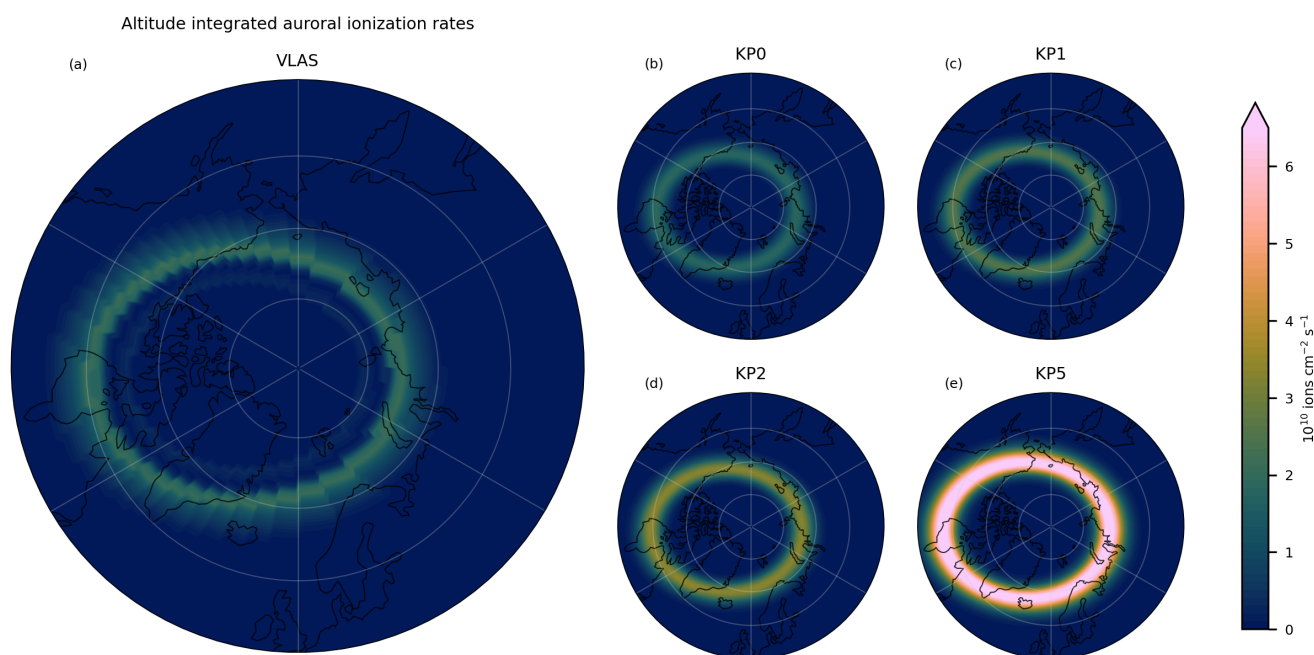
Figure 4. Vertically integrated auroral ionization rates, as output from WACCM-D on geographic coordinates for the northern hemisphere (geographic latitude > $50°$N), 1 Jan 2006. (a) VLAS, (b) KP0, (c) KP1, (d) KP2 (e) KP5.

Comparisons of the ionization rates from eVlasiator and the Kp parameterization are shown in Figs. 4–5 for the northern hemisphere. The vertically integrated ionization rates in Fig. 4 show the full auroral oval. While the eVlasiator-derived auroral ionization rates roughly match the location of the Kp-driven ionization rates, the oval is much more sharply defined than the parameterized auroral precipitation. The sharpness can also be seen in the latitudinal extent of the aurora in Fig. 5, which shows

225 the logarithm of the ionization rates at longitude $90°$E for the VLAS and KP2 runs. The auroral ionization rates peak at roughly the same latitude, but the Kp parameterization has a much wider latitudinal spread. This difference in extent results from the limitation in the latitudinal coverage made possible by the used eVlasiator run, as the cutoff latitude of $63°$ MLAT corresponds to the mapping of the innermost considered locations in the magnetospheric domain ($4.8\,R_\mathrm{E}$; see Appendix A). In future runs
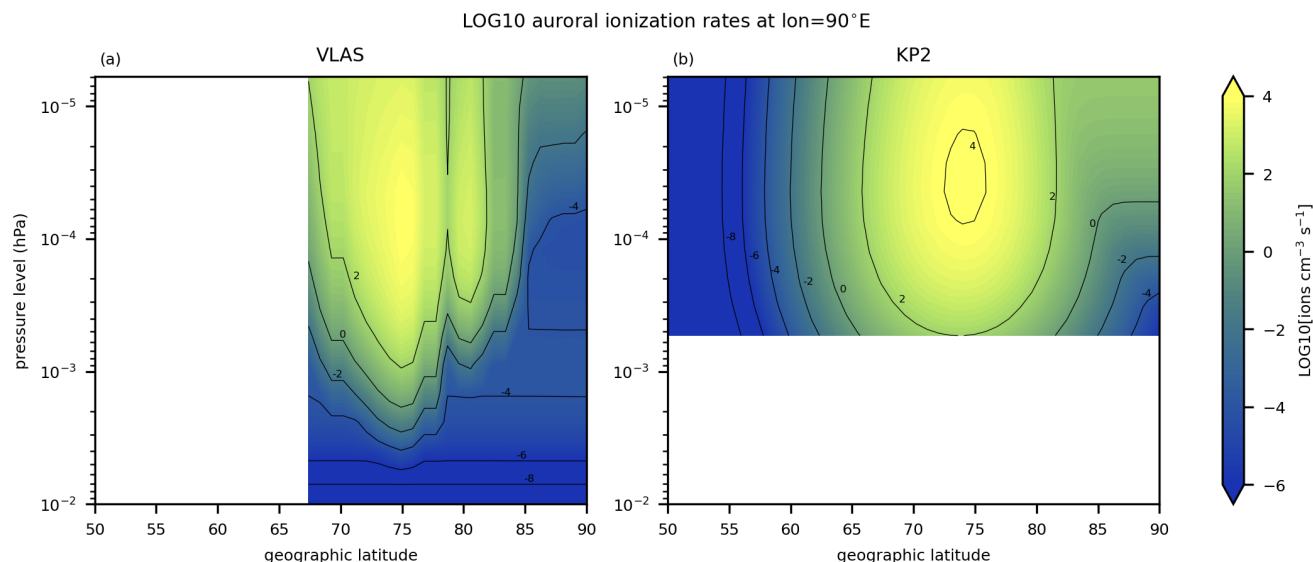
Figure 5. The geographic latitude–altitude extent of the auroral electron forcing output from WACCM-D simulation runs (a) VLAS and (b) KP2 on 1 Jan 2006. The LOG10 of the auroral ionization rates at longitude $90°$E.

with an inner boundary closer to the Earth's surface, this sharp cutoff near the auroral oval's equatorward boundary could be
230 avoided. The eVlasiator ionization rates also have a slight secondary peak on the poleward side, while the Kp parameterization clearly only has one peak.

The eVlasiator auroral ionization forcing reaches deeper into the atmosphere down to around $0.01\,\text{hPa}$ ($\sim$80 km), while the Kp parameterization stops at around $5 \times 10^{-4}\,\text{hPa}$ ($\sim$95 km), the lower boundary of the parameterization. Though the eVlasiator ionization rates are negligible at the $0.01\,\text{hPa}$ level, the tapering off of the aurora towards lower altitudes is more
235 gradual compared to the Kp parameterization.

3.2 Atmospheric impact

Figure 6 shows the polar cap-averaged (geographic latitude $> 60°$), altitude-integrated NO_x response in the auroral runs relative to the REF run with no auroral electron forcing. For both SH and NH we clearly see the NO_x impact during the winter season for all the auroral forcing scenarios. The effect is naturally strongest in the thermosphere, where the auroral electrons have a direct
240 impact, with the eVlasiator auroral precipitation causing a NO_x increase of up to 200 % in the SH lower thermosphere ($\sim$85–125 km). The descent of the produced NO_x can also clearly be seen in the mesosphere ($\sim$50–85 km) and upper stratosphere ($\sim$25–50 km). The descent is seen in the lag when comparing the peak occurrence times, as the strongest SH thermospheric, mesospheric, and stratospheric NO_x impacts occur in June, July, and August, respectively. The impact also grows weaker during the descent, since the background levels of NO_x are higher at lower altitudes, and not all the produced NO_x descends.
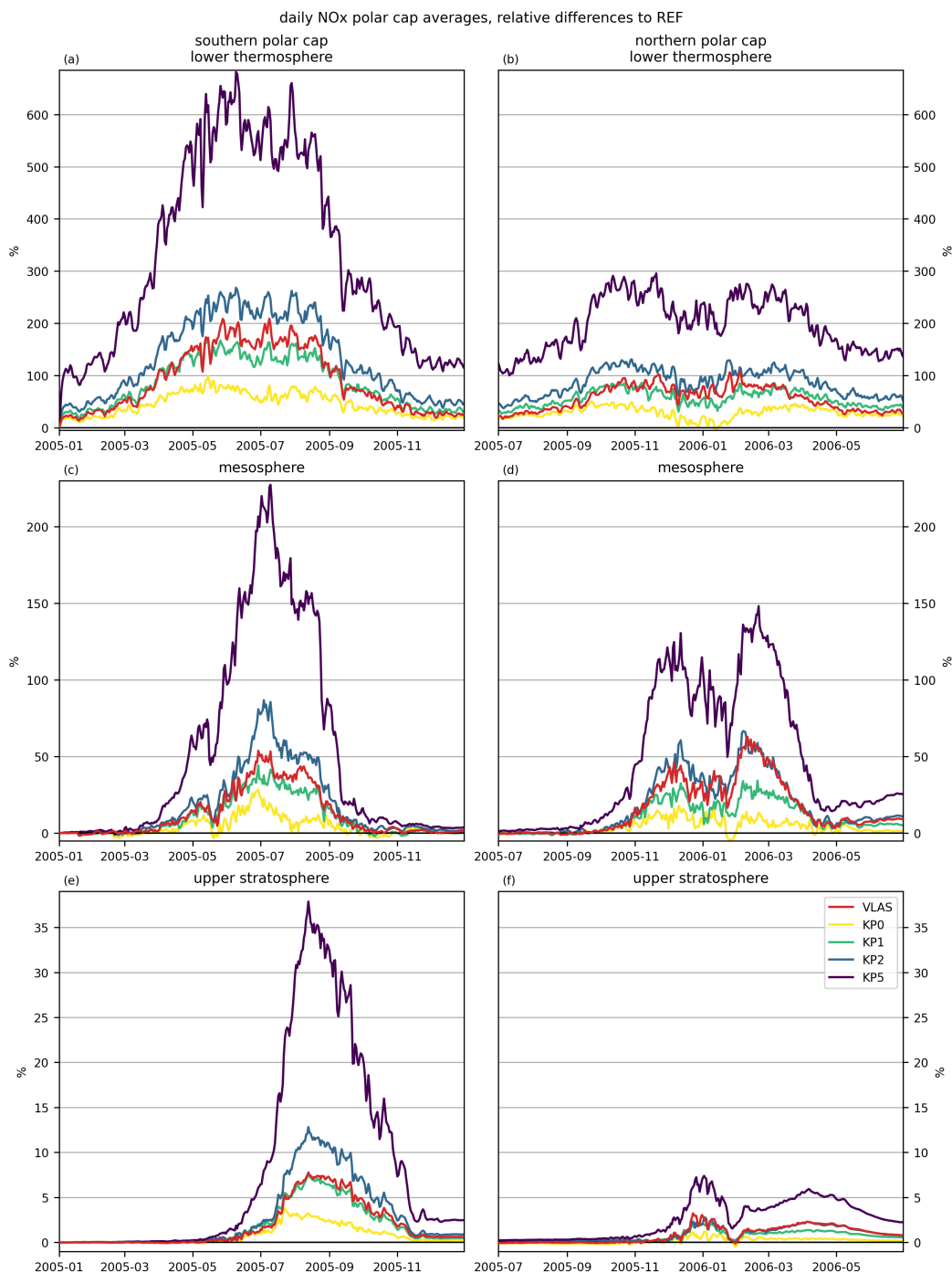
Figure 6. Auroral impact on NO_x concentrations: Polar cap (geographic latitude $> 60°$) averages of the integrated (a–b) lower thermosphere, (c–d) mesosphere, and (e–f) upper stratosphere for the (a, c, e) SH and (b, d, f) NH winters. Relative difference of the auroral precipitation simulation runs (colours) compared to the REF run with no auroral electron forcing. Lower thermosphere integrated from $3 \times 10^{-3}\,\text{hPa}$ to $1 \times 10^{-5}\,\text{hPa}$ ($\sim$85–125 km), mesosphere from $1\,\text{hPa}$ to $3 \times 10^{-3}\,\text{hPa}$ ($\sim$50–85 km), and upper stratosphere from $30\,\text{hPa}$ to $1\,\text{hPa}$ ($\sim$25–50 km).

245   Comparing the Kp-driven auroral precipitation runs, there is a clear scaling effect: the NO_x impact grows stronger with increasing Kp. Even in the KP0 case the SH lower thermospheric NO_x is increased by more than 90%, with KP5 reaching an increase of 680% in the SH. The eVlasiator aurora run (VLAS) corresponds to the KP1 and KP2 simulations in terms of the NO_x impact, often coming closer to the KP1 scenario. This is despite the eVlasiator electron fluxes being calibrated using DMSP observations during Kp index values of ~2–3, and the Kp index being fixed to 2 for the VLAS WACCM-D simulation.

250 While the VLAS impact does occasionally reach the KP2 level, with the NH mesospheric and upper stratospheric responses being very similar between the two simulations, it is possible that the parameterization is overestimating the auroral electron forcing at low Kp values.

     The strongest impacts are consistently seen in the southern hemisphere. The differences between the hemispheres can be explained by the instability of the polar vortex in the NH, as well as the sudden stratospheric warming (SSW) that occurred in

255 mid-January 2006 (Manney et al., 2008; Butler et al., 2015). This is likely the cause of the double peaks in the NO_x impact in the NH, since the anomalous dynamical conditions due to SSW result in higher NO_x levels also in the REF simulation, so the relative differences are smaller during the SSW. Later in the winter strong downward transport resumed and caused a sharp increase of NO_x in the mesosphere (Randall et al., 2009), which is also seen in our simulations.

     For more details on the spatial distribution of the auroral precipitation NO_x impact, Fig. 7 shows the REF wintertime

260 averages in both hemispheres, and the increase in the VLAS simulation relative to REF. From the REF number densities we see that there is a difference in the NO_x vertical profiles between the hemispheres. In the north, NO_x has a polar peak at thermospheric altitudes, but in the south the peak is located lower, in the mesosphere. The occurrence of a solar proton event in mid-May 2005 likely contributes to the SH peak, as the proton precipitation penetrates to mesospheric altitudes. The increased NO_x production and the longer chemical lifetime in the winter pole allows NO_x to accumulate in the SH mesosphere. In the

265 NH the SSW may also be leading to disruption in the vertical transport of NO_x so that a greater proportion of produced NO_x stays in the thermosphere rather than being transported downward.

     In the SH the NO_x is rather symmetrically distributed around the pole. Since the southern polar vortex is very stable, and there is no auroral precipitation, the NO_x production in the thermosphere is driven by solar radiation. On the other hand, in the NH the peaks and troughs are distributed off-pole, and there are shifts in spatial location between the altitude layers. This is

270 caused by the less stable nature of the NH polar vortex. The SSW that occurred during the 2005–2006 NH winter likely adds to the effect.

     In the VLAS run, NO_x is clearly increased throughout the thermosphere and mesosphere, and not just in the auroral oval latitudes, as NO_x is transported from the production region. In the upper stratosphere, the impact is confined inside the polar vortex latitudes with little impact outside it. The SH lower thermosphere does show the effect of the electron precipitation within

275 the auroral oval, with the strongest NO_x responses reaching over 200 %, corresponding to Fig. 6a. The NH thermospheric NO_x response in much weaker than the SH, and the auroral oval pattern can only be distinguished on the North American longitude sector. The weaker response and its longitude distribution can overall be explained by the higher REF levels of NO_x in the NH and the location of the NH thermospheric NO_x peak over the Eurasian longitude sector, respectively.
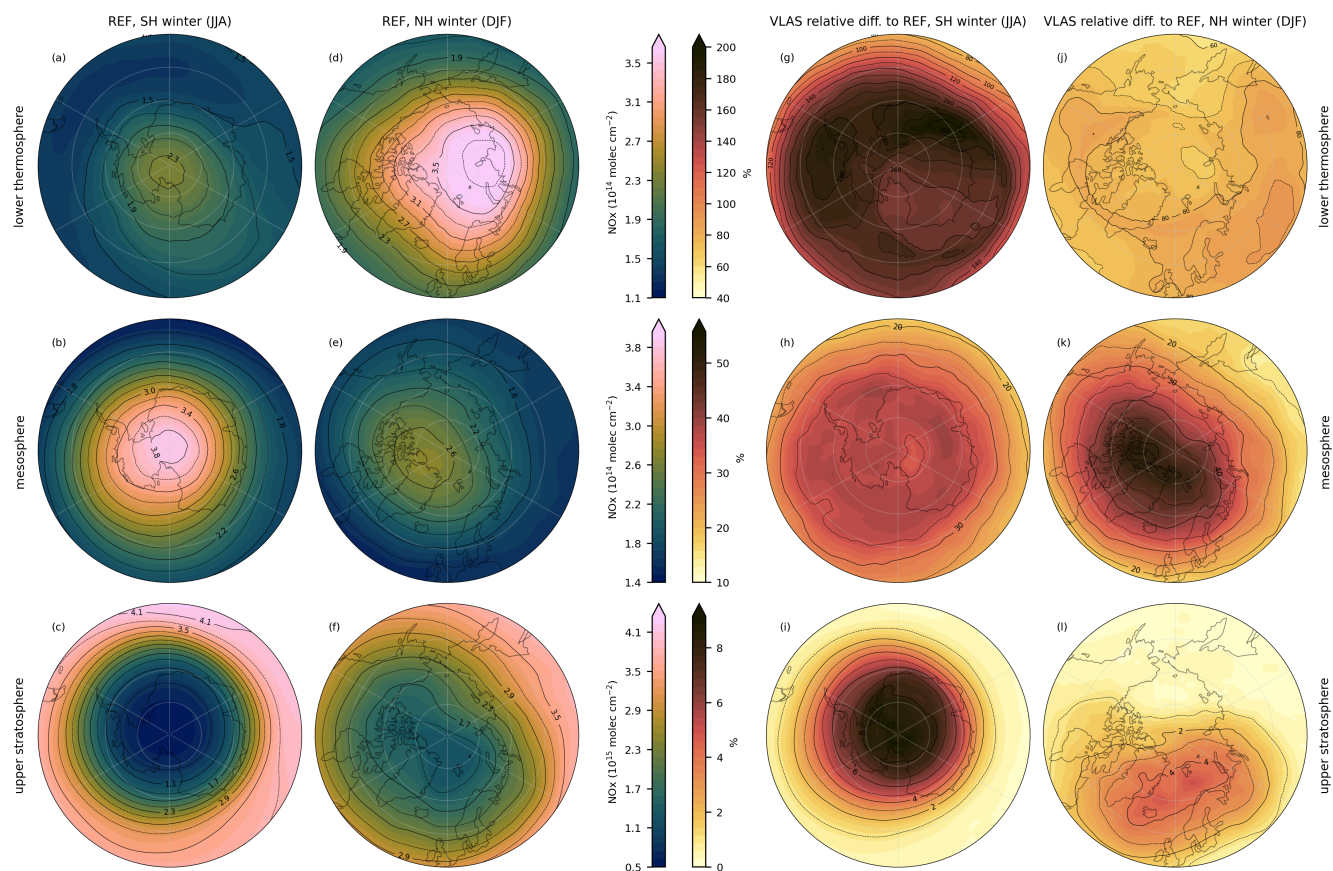
Figure 7. (a–f) Altitude integrated REF NO_x number densities and (g–l) the relative NO_x impact of the VLAS simulation compared to REF, for (a–c, g–i) SH and (d–f, j-l) NH polar regions (geographic latitude $> 50°$). Both the the concentrations and relative differences are averaged over the winter seasons (Jun–Aug 2005 for SH, Dec 2005–Feb 2006 for NH). The atmospheric layers – (a, d, g, j) lower thermosphere, (b, e, h, k) mesosphere, and (c, f, i, l) upper stratosphere – correspond to Fig. 6.

In the mesosphere, the relative auroral precipitation impact is stronger in the NH, again explained by the difference in the
280 REF background levels. This corresponds well to the mesospheric VLAS impacts in Fig. 6c–d. Stratospheric impacts show again the differences in the REF NO_x number densities. The SH shows clearly the impact centred around the pole, since the NO_x produced by the auroral precipitation descends within the polar vortex from thermospheric altitudes to the startosphere. In the NH the VLAS auroral electron impact in the stratosphere has a more irregular form, and it is located off-pole, showing the less stable polar vortex.

285 The upper stratospheric ozone responses to the auroral electron forcing scenarios are shown in Fig. 8. The O_3 impact is much weaker than NO_x, and comparing the KP5 SH results from Fig. 6, and Fig. 8, we see that a NO_x increase of over 600 % in the lower thermosphere leads to an increase of around 35 % NO_x in the upper stratosphere, corresponding to a reduction in upper
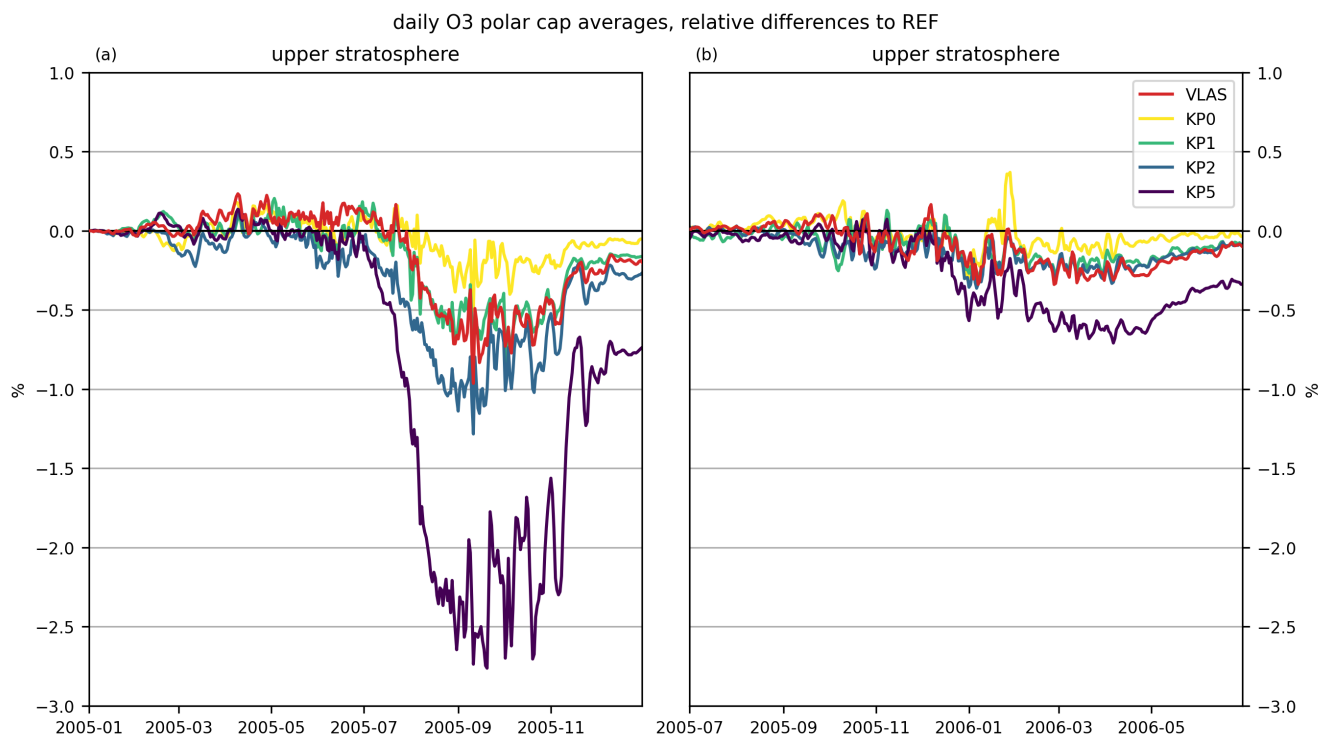
Figure 8. Upper stratospheric ozone response to auroral electron forcing: daily relative difference in vertically integrated ozone number densities from the auroral precipitation simulation runs (colours) compared to the REF run with no auroral precipitation. Polar cap averages (geographic latitude > 60°) for (a) SH and (b) NH winters.

stratospheric O_3 by only 2.5 %. Similarly for the VLAS run, we see an increase of up to 200 % in the lower thermospheric NO_x, which results in a decrease of around 0.7 % in upper stratospheric ozone. As with NO_x, the ozone impact is stronger in the SH, and the NH upper stratospheric impact is less than 0.8 % even in the KP5 case when compared to no auroral electron forcing.

4 Discussion

Our results demonstrate a successful interfacing of magnetospheric and atmospheric simulations. We are able to produce realistic auroral electron precipitation fluxes from eVlasiator, and they have been applied as auroral electron forcing in the WACCM model. The simulated electron fluxes produce atmospheric impacts comparable to WACCM's current auroral electron parameterization, but with enhanced information on energy and spatial distribution. Thus this work presents the potential for future studies on the interaction between the solar wind and the atmosphere, e.g., for the study of the atmospheric impacts of magnetospheric substorms. Eventually, atmospheric forcing could be driven directly by solar wind parameters instead of

proxy-based parameterizations built on limited magnetospheric electron flux data. In the future, this would also make way
for near-real-time predictions of the atmospheric response. First steps towards this include the production of time-dependent
auroral electron precipitation forcing from the magnetospheric simulations, on an extended temporal scale more useful to
long-term atmospheric simulations.

Our results also indicate that the current parameterization of aurora may be overestimating the auroral forcing, at least at
low Kp index values. Further studies are needed to ascertain the correct level of auroral electron forcing, including eVlasiator
simulations of the auroral electron fluxes during periods of higher Kp indices. Satellite observations of NO_x species could
be used to study the accurate levels of NO_x production that should result from auroral electrons. In addition, electrons at
energies beyond the auroral range (> 50keV) should also considered, e.g. through the inclusion of reconnection and radiation
belt processes in future versions of Vlasiator. This could aid in bridging the gap between auroral and medium-energy electrons.

Limitations of the magnetospheric models should also be considered. As pointed out in Sect. 2.3.1, eVlasiator does not model
all sources of precipitating auroral electrons, an therefore underestimated the total precipitating fluxes. We have mitigated the
effect of this underestimation in this study by using the DMSP observations to calibrate the electron fluxes. The latitudinal
extent of the eVlasiator-derived auroral precipitation is also limited compared to the Kp parameterization, arising from the
distance of the eVlasiator run's inner boundary from the surface of the Earth. We have not considered this limitation in the
interpretation of the atmospheric impacts of the precipitation. Auroral ionization rates for future eVlasiator simulations with a
less sharp cutoff on the equatorward side of the auroral oval will therefore likely provide an enhancement in the NO_x response,
and, as seen in Fig. 7, the NO_x impact is not limited to the auroral oval region.

5 Conclusions

In this study we have demonstrated for the first time a novel approach to investigating the role of auroral electron precipitation
in the MLTI. We used eVlasiator to simulate electron precipitation fluxes at auroral energies (50 eV–50 keV) that were scaled
using satellite observations to account for deficiencies in the magnetospheric model. Ionization rates derived from the electron
fluxes were then used as input in WACCM-D in order to analyze the atmospheric NO_x and ozone impacts of the auroral
electron precipitation. We found the strongest response in the SH polar lower thermosphere, where the eVlasiator-derived
auroral precipitation increased NO_x concentrations up to 200 %. In the mesosphere there was an increase of more than 50 % in
NO_x in both hemispheres. The auroral precipitation response can also be seen in the upper stratosphere, where we see a NO_x
increase of around 7 %, which corresponds to a peak decrease of 0.7 % in upper stratospheric ozone.

As comparison to the eVlasiator-derived auroral precipitation we used WACCM's parameterization of auroral electron forc-
ing, which is driven by the Kp index. Overall, the electron precipiation from eVlasiator is similar to the parameterized auroral
electron forcing in location and impact, although there are some clear differences. The latitudinal extent of the eVlasiator au-
roral electron precipitation is partially limited, and the ionization rates are somewhat weaker than the parameterization, even
with the satellite observation-based scaling of the electron fluxes. On the other hand eVlasiator provides more detailed energy

and spatial distributions of the auroral electron precipitation, with ionization forcing reaching deeper in to atmosphere, down to $80\,\mathrm{km}$ compared to around $95\,\mathrm{km}$ in the parameterization.

As a next step, in order to validate the accuracy of the model results, a specific simulation could be made for comparisons with satellite observations. For this, time-dependent auroral electron precipitation data from eVlasiator would be needed in
335   order to model the variability of auroral electron impact in the atmosphere. For example, we should study impacts during the different phases of substorms. For the future, this work makes way for a more complete description of auroral electron forcing in atmospheric simulations and, eventually, for the detailed study of solar wind – atmosphere interaction.

Code and data availability. The Vlasiator code is open-source under GPL-2, indexed through Zenodo (Pfau-Kempf et al., 2024), and available through GitHub. The eVlasiator release used for this study is similarly available at Pfau-Kempf et al. (2022). The Vlasiator simulation
340   data used for this study consists of several terabytes of data, and is thus not made available online, but the authors accept data requests. The reduced output of the eVlasiator simulation consisting of precipitating electron differential number flux data is available at Finnish Meteorological Institute Research Data repository METIS (Grandin, 2024).

The DMSP/SSJ precipitating particle fluxes are openly available and were retrieved from http://cedar.openmadrigal.org/.

WACCM-D simulation data analysed in this paper are available at Finnish Meteorological Institute Research Data repository METIS
345   (Häkkilä and Szelag, 2024). The WACCM modification enabling MLT-dependent ionization input is indexed via Zenodo (Häkkilä, 2024), and publicly available on GitHub at https://github.com/hakkila/waccm_iprmlt.

Appendix A: Detailed description of the mapping between the ionosphere grid and the eVlasiator simulation domain

To produce an auroral-electron forcing dataset for WACCM-D, we need to map the fluxes obtained with eVlasiator to ionospheric altitudes. The procedure detailed below is illustrated in Fig. A1.
350   Magnetic field lines (in magenta) are traced between the ionosphere (at an altitude of $110\,\mathrm{km}$; points A_i) and the inner boundary of the simulation domain from seed points placed every $1°$ in MLAT and $0.5\,\mathrm{h}$ in MLT. Since the magnetic field inside the inner boundary only consists of the Earth dipole and has no perturbed field term, we construct a more realistic mapping by superposing two magnetic field components. The internal contributions to the geomagnetic field are described by a simple point dipole to match the geomagnetic field description used in Vlasiator. The Tsyganenko 2001 (T01; Tsyganenko,
355   2002a, b) model is used to describe the external field contributions, with the solar wind conditions of the Vlasiator run (see Sect. 2.1), at a date when the geomagnetic dipole was almost perpendicular to the ecliptic plane (11 March 2020, 21:40 UT), and assuming a Dst value of $-30\,\mathrm{nT}$. The Python versions of T01 and Earth dipole field implemented in the geopack library (Tian, 2023) were used for this mapping of atmospheric altitudes to $4.8\,R_\mathrm{E}$, i.e. just beyond the inner boundary (points B_i). From each grid point, we follow the geomagnetic field line obtained by combining the untilted dipole model for internal
360   contributions with the T01 model for external contributions. Up to this step, the procedure is the same as described in more detail in Grandin et al. (2023).
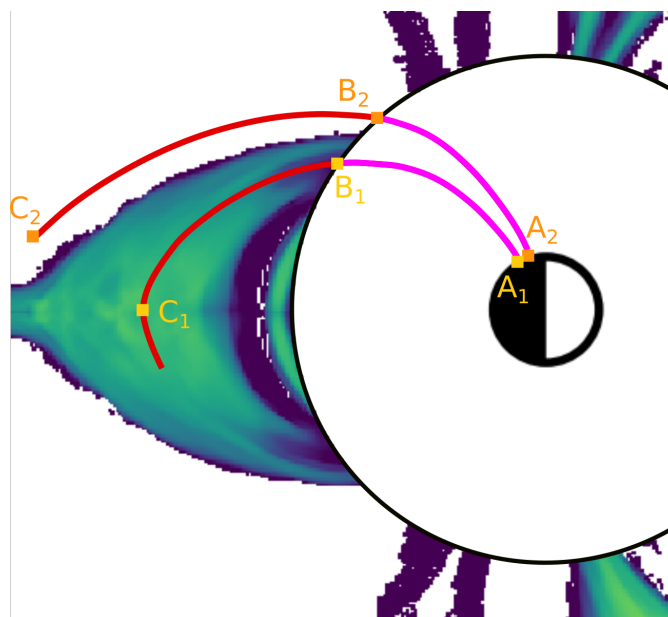
Figure A1. Illustration of the mapping of eVlasiator precipitating electron fluxes to ionospheric altitudes. The view is a slice of the eVlasiator domain in the noon–midnight meridional plane, with the Sun located to the right of the figure. Points A_1 and A_2 are located on the ionospheric grid (Cartesian in MLAT–MLT) at 110 km altitude. Points B_1 and B_2 are located next to the eVlasiator domain's inner boundary at 4.8 R_E. The magenta lines indicate the superposition of a non-tilted dipole field with the T01 model. The red lines follow the magnetic field within the eVlasiator domain. Point C_1 is located in the equatorial plane, and point C_2 is located at a distance of 7.5 R_E from point B_2 along the magnetic field line.

Within the 1.4 s of the eVlasiator run, electrons scattered into the bounce loss cone in the plasma sheet do not have time to reach the inner boundary of the simulation domain. To account for this, we extend the mapping of the MLT–MLAT grid further into the eVlasiator simulation domain so as to reach the magnetospheric regions where precipitating electrons originate. To
365 ensure better self-consistency, we use the magnetic field lines from the Vlasiator file (in red) to extend the mapping outwards for another 7.5 R_E, or until reaching the equatorial plane.

Finally, along each field line thus obtained and for each electron energy bin, the maximum value of the precipitation differential flux between the inner boundary (points B_1, B_2) and either the other end of the traced field line (point C_2) or the equatorial plane (point C_1) is retained. This therefore ensures that precipitating electrons which may not have had time to reach the inner
370 boundary by the end of the electron simulation are taken into account, and gives a conservative high value for the differential number flux.

Figure B1. Comparison of eVlasiator and DMSP/SSJ observations during the 1 Aug 2011 overpasses. (a–b) Integrated energy flux of precipitating electrons obtained with eVlasiator (background) on top of which corresponding measurements by DMSP/SSJ are overlaid along the spacecraft's orbits. (c–d) Differential number fluxes along the orbit for eVlasiator (background colour) and DMSP/SSJ (contours). (e–f) Ratio between DMSP/SSJ and eVlasiator differential number fluxes along the orbits.

Appendix B: Detailed description of the calibration of eVlasiator electron fluxes with DMSP/SSJ observations

B1 Comparison of eVlasiator fluxes along the DMSP orbits

Figures B1 and B2 show the comparison of eVlasiator precipitating electron fluxes with DMSP/SSJ measurements during
375 the two events with similar driving conditions as in the Vlasiator run (8 Aug 2011 and 10 Oct 2015). The top panels show
the global view of eVlasiator integrated energy fluxes in both hemispheres, on top of which DMSP/SSJ integrated energy
fluxes along the spacecraft's orbits are overlaid. The middle panels enable the comparison of differential number fluxes of
precipitating electrons. One can see in particular that overall eVlasiator spectra have a cutoff at high energies, indicating that
the high-energy component is often missing compared to DMSP/SSJ observations.

380   The bottom panels show the ratio between the differential number fluxes measured by DMSP/SSJ and obtained with eVlasia-
tor are displayed, along the satellites' orbits. Green regions correspond to eVlasiator underestimating the electron precipitation,
whereas purple regions correspond to eVlasiator overestimating it, when considering a given event and location along the orbit.

Figure B2. Comparison of eVlasiator and DMSP/SSJ observations during the 10 Oct 2015 overpasses. Same format as in Fig. B1.

The ratios typically range between 0.001 and 1000, highlighting the need for a calibration of the eVlasiator fluxes so that they might be more realistic. It is clear from those bottom panels that the correction to be applied to eVlasiator fluxes must be different on the dayside and on the nightside, and that it must be energy-dependent. Below we detail how the corrected eVlasiator fluxes were determined and we justify the choices made in developing the method.

B2 Selection of regions of interest to be corrected

In order to avoid increasing the precipitating electron fluxes outside of the auroral oval (e.g. in the polar cap or in the flanks, where eVlasiator fluxes might be contaminated by boundary effects), we restrict the correction to the cusp and nightside oval regions, as indicated with magenta contours in Fig. B3a–b. Besides, extremely low eVlasiator flux values ($< 0.01\,\mathrm{el\,cm^{-2}\,s^{-1}\,sr^{-1}\,eV^{-1}}$) are masked too.

Since the dayside overpasses include measurements outside the hence delimited cusp, we discard observations made outside of the cusp for the calibration procedure. The masked data are shown in grey in Fig. B3c,e.
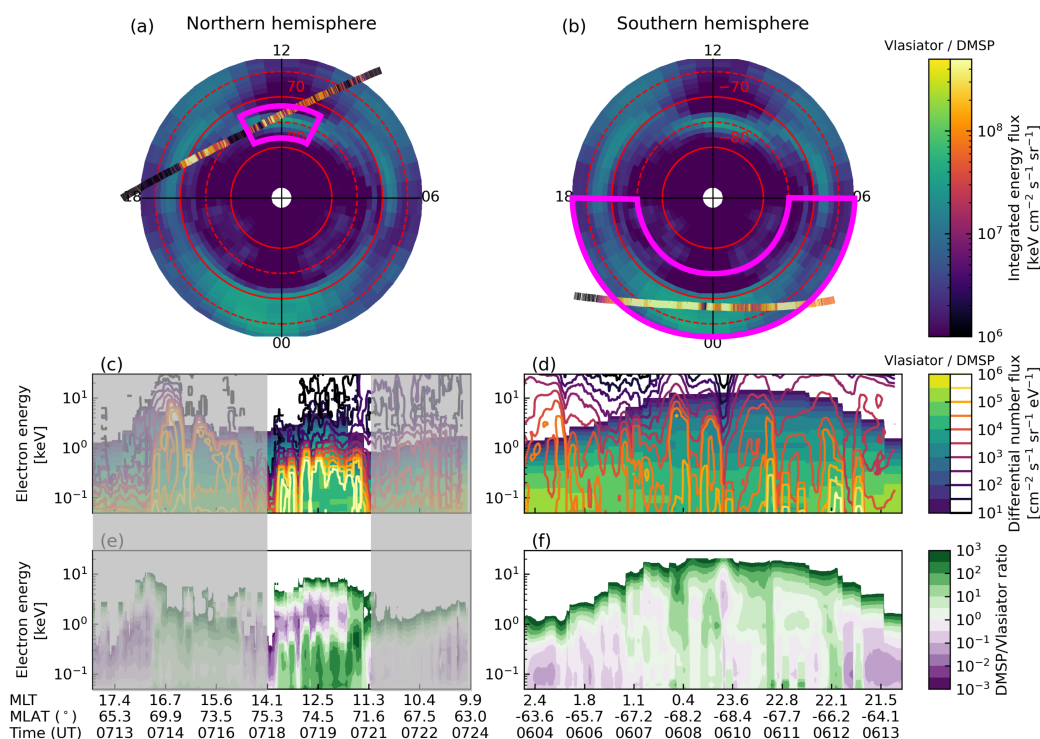
Figure B3. Same as Fig. B1 with regions of interest (cusp and nightside oval) indicated in magenta in panels a–b. The grey shading in panels c and e indicates the masking used for the dayside overpass, to keep only cusp measurements.

B3   Quantile fitting for DMSP/eVlasiator flux ratios

395   Since we want to obtain correction coefficients for the eVlasiator fluxes as a function of electron energy, we need to find a suitable metrics to derive such coefficients based on the ratios between DMSP and eVlasiator fluxes along the DMSP orbits. A quick inspection of Fig. B3e–f reveals that using the mean value of the ratio at a given energy would not provide a robust estimate of the needed correction, since for instance at 1 keV on the nightside values range from 10^3 (start of the orbit) to $< 1\,\mathrm{el}\,\mathrm{cm}^{-2}\,\mathrm{s}^{-1}\,\mathrm{sr}^{-1}\,\mathrm{eV}^{-1}$ (middle of the orbit), which would result in a mean value skewed to the high values and not

400   necessarily representative of the needed correction coefficient at 1 keV. This is because the eVlasiator fluxes drop off quickly at the high-energy end of their spectra, due to the sparse velocity space description (Palmroth et al., 2018). Therefore, instead of using the mean, we use a quantile value as the metrics to determine the energy-dependent correction coefficients (one set for cusp fluxes, one set for nightside fluxes).

Figure B4 shows results obtained when considering median (50th quantile) values. We see that the median values of the ratios

405   (blue lines) can be fitted with a third-order polynomial for the cusp and with a second-order polynomial for the nightside (red curves), when considering energies and ratios in logarithmic scale. We can then correct the eVlasiator fluxes by multiplying
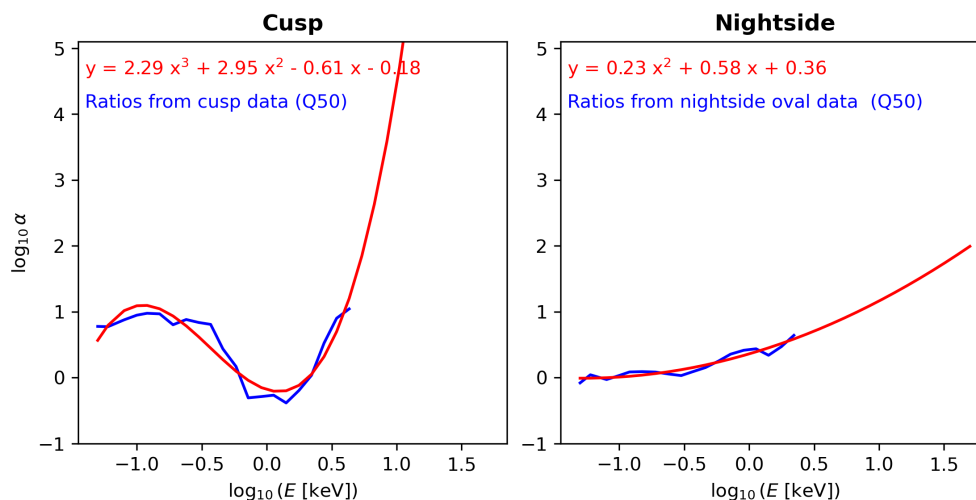
Figure B4. Energy-dependent correction coefficients obtained for the cusp (left) and nightside (right) eVlasiator fluxes obtained by taking the median (Q50) values of the DMSP/eVlasiator flux ratios. The red lines indicate polynomial fits of the data-based curves in blue.

them with those analytical (polynomial) energy-dependent expressions, in the entire regions of interest (cusp and nightside oval).

B4   Adjustment based on the integrated energy fluxes

410   The median-based corrections presented above lead to an enhancement of the eVlasiator fluxes in a way which gives priority to increasing the energies needing it the most to better resemble observations. However, this increase is still insufficient. Indeed, if we consider the ratio of the corrected eVlasiator and DMSP integrated energy fluxes along the satellite orbits, we find that its 90th quantile values are 0.18 in the cusp and 0.24 in the nightside oval, which means that the corrected eVlasiator fluxes are still 4–5 times lower than in observations using this metrics.

415   Therefore, we have adopted the following strategy to obtain corrected eVlasiator fluxes providing a good match with DMSP/SSJ measurements in terms of integrated energy flux: instead of taking median values of the DMSP/eVlasiator ratios to determine the analytical expression of the energy-dependent correction coefficients, we find the optimal quantiles of these ratios such that the integrated energy fluxes match as closely as possible between corrected eVlasiator fluxes and observations.

We found that selecting the 61st (cusp) and 67th (nightside) quantiles of the DMSP/eVlasiator differential flux ratios along

420   the orbits give the best results, with corrected eVlasiator precipitation being on par with DMSP/SSJ observations in terms of integrated energy fluxes. The corresponding correction coefficients are given in Fig. B5.

Those coefficients were therefore retained for the eVlasiator flux correction, and produced the corrected fluxes shown in Fig. 3.
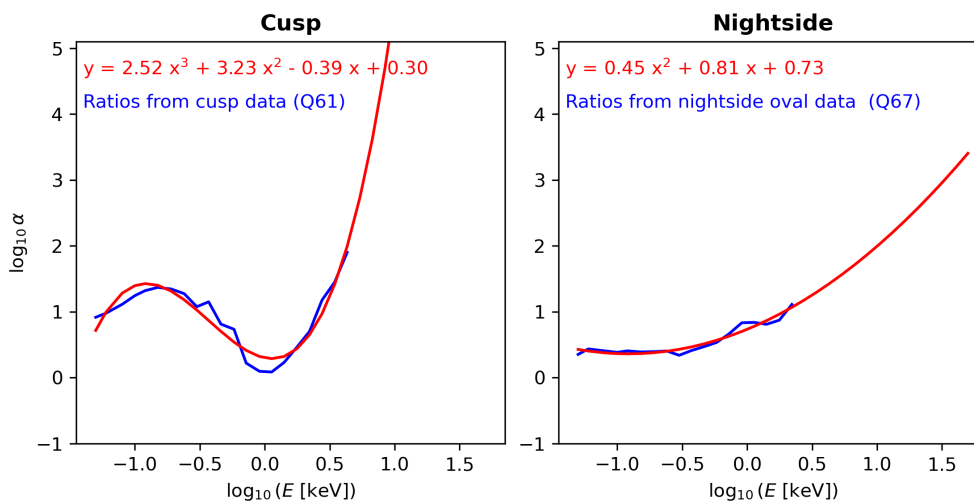
Figure B5. Same as Fig. B4 but using the 61st quantile of the DMSP/eVlasiator flux ratios for the cusp and the 67th quantile for the nightside fluxes.

Author contributions. MB and MA developed the eVlasiator approach, with LK extending it to support 3D spatial meshes. MA ran the
425 eVlasiator simulation presented in this work. MG developed the particle precipitation approach of Vlasiator, applied it to the eVlasiator
data, implemented the ionospheric mapping and calibration approaches presented in the appendices and used in this study, and wrote the
corresponding sections of the manuscript. MP is the Vlasiator PI, and she participated in conceptualisation of the study, and supervised the
Vlasiator portion of the study. TH, MES, NK, and PTV participated in planning the WACCM-D simulations. TH carried out the WACCM-
D simulations with support from MES. PTV produced the ionization rates used in WACCM-D from the eVlasiator electron fluxes. TH
430 analyzed the WACCM-D data and led the writing of the paper, with all co-authors participating in discussions and providing feedback on the
manuscript.

Competing interests. At least one of the (co-)authors is a member of the editorial board of Annales Geophysicae.

Acknowledgements. We gratefully acknowledge the DMSP/SSJ community and data stewards and services for providing observations of
precipitating particle fluxes. The work of MG is funded by the Research Council of Finland (grant 338629-AERGELC'H). We acknowledge
435 the Research Council of Finland grant 335554-ICT-SUNVAC, and Finnish Centre of Excellence in Research of Sustainable Space (grant
number 352846).
Vlasiator development acknowledges European Research Council starting grant 200141-QuESpace and Consolidator grant 682068-
PRESTISSIMO. The CSC–IT Center for Science in Finland and the PRACE Tier-0 supercomputer infrastructure in HLRS Stuttgart (grant
nos. PRACE-2012061111 and PRACE-2014112573) are acknowledged as they made these results possible. The Vlasiator team wishes to

440   thank the Finnish Grid and Cloud Infrastructure (FGCI) and specifically the University of Helsinki computing services for supporting this project with computational and data storage resources.

The scientific colour maps *batlow* and *lajolla* (Crameri, 2023) are used in this study to prevent visual distortion of the data and exclusion of readers with colour-vision deficiencies (Crameri et al., 2020).

PTV, MG, and NK would like to thank the CHAMOS team for useful discussions (https://chamos.fmi.fi).

References

Alho, M., Battarbee, M., Pfau-Kempf, Y., Khotyaintsev, Y. V., Nakamura, R., Cozzani, G., Ganse, U., Turc, L., Johlander, A., Horaites, K., Tarvus, V., Zhou, H., Grandin, M., Dubart, M., Papadakis, K., Suni, J., George, H., Bussov, M., and Palmroth, M.: Electron Signatures of Reconnection in a Global eVlasiator Simulation, Geophysical Research Letters, 49, e98 329, https://doi.org/10.1029/2022GL098329, 2022.

Andersson, M. E., Verronen, P. T., Marsh, D. R., Päivärinta, S.-M., and Plane, J. M. C.: WACCM-D – Improved modeling of nitric acid and active chlorine during energetic particle precipitation, J. Geophys. Res. (Atmos.), 121, 10,328–10,341, https://doi.org/10.1002/2015JD024173, 2016.

Barth, C. A., Baker, D. N., and Mankoff, K. D.: The northern auroral region as observed in nitric oxide, Geophys. Res. Lett., 28, 1463–1466, 2001.

Battarbee, M., Brito, T., Alho, M., Pfau-Kempf, Y., Grandin, M., Ganse, U., Papadakis, K., Johlander, A., Turc, L., Dubart, M., and Palmroth, M.: Vlasov simulation of electrons in the context of hybrid global models: an eVlasiator approach, Annales Geophysicae, 39, 85–103, https://doi.org/10.5194/angeo-39-85-2021, 2021.

Butler, A. H., Seidel, D. J., Hardiman, S. C., Butchart, N., Birner, T., and Match, A.: Defining sudden stratospheric warmings, Bulletin of the American Meteorological Society, 96, 1913–1928, 2015.

Crameri, F.: Scientific colour maps, https://doi.org/10.5281/zenodo.8409685, 2023.

Crameri, F., Shephard, G. E., and Heron, P. J.: The misuse of colour in science communication, Nature Communications, 11, 5444, https://doi.org/10.1038/s41467-020-19160-7, 2020.

Damiani, A., Funke, B., Santee, M. L., Cordero, R. R., and Watanabe, S.: Energetic particle precipitation: A major driver of the ozone budget in the Antarctic upper stratosphere, Geophys. Res. Lett., 43, 3554–3562, https://doi.org/10.1002/2016GL068279, 2016.

Dubart, M., Ganse, U., Osmane, A., Johlander, A., Battarbee, M., Grandin, M., Pfau-Kempf, Y., Turc, L., and Palmroth, M.: Resolution dependence of magnetosheath waves in global hybrid-Vlasov simulations, Annales Geophysicae, 38, 1283–1298, https://doi.org/10.5194/angeo-38-1283-2020, 2020.

Fang, X., Randall, C. E., Lummerzheim, D., Wang, W., Lu, G., Solomon, S. C., and Frahm, R. A.: Parameterization of monoenergetic electron impact ionization, Geophys. Res. Lett., 37, L22 106, https://doi.org/10.1029/2010GL045406, 2010.

Funke, B., López-Puertas, M., Stiller, G. P., and von Clarmann, T.: Mesospheric and stratospheric NO_y produced by energetic particle precipitation during 2002–2012, J. Geophys. Res., 119, 4429–4446, https://doi.org/10.1002/2013JD021404, 2014.

Ganse, U., Koskela, T., Battarbee, M., Pfau-Kempf, Y., Papadakis, K., Alho, M., Bussov, M., Cozzani, G., Dubart, M., George, H., Gordeev, E., Grandin, M., Horaites, K., Suni, J., Tarvus, V., Kebede, F. T., Turc, L., Zhou, H., and Palmroth, M.: Enabling technology for global 3D + 3V hybrid-Vlasov simulations of near-Earth space, Physics of Plasmas, 30, 042 902, https://doi.org/10.1063/5.0134387, 2023.

Gettelman, A., Mills, M. J., Kinnison, D. E.and Garcia, R. R., Smith, A. K., Marsh, D. R., Tilmes, S., Vitt, F., Bardeen, C. G., McInerny, J., Liu, H.-L., Solomon, S. C., Polvani, L. M., Emmons, L. K., Lamarque, J.-F., Richter, J. H., Glanville, A. S., Bacmeister, J. T., Phillips, A. S., Neale, R. B., Simpson, I. R., DuVivier, A. K., Hodzic, A., and Randel, W. J.: The whole atmosphere community climate model version 6 (WACCM6), J. Geophys. Res. (Atmos.), 124, 12 380–12 403, https://doi.org/10.1029/2019JD030943, 2019.

Grandin, M.: eVlasiator 3D run (eEGI-1506) with DMSP correction: Precipitating electron differential number flux data, https://doi.org/10.57707/FMI-B2SHARE.79A154A9959347D0829B0AB2E145499C, 2024.

Grandin, M., Battarbee, M., Osmane, A., Ganse, U., Pfau-Kempf, Y., Turc, L., Brito, T., Koskela, T., Dubart, M., and Palmroth, M.: Hybrid-Vlasov modelling of nightside auroral proton precipitation during southward interplanetary magnetic field conditions, Annales Geophysicae, 37, 791–806, https://doi.org/10.5194/angeo-37-791-2019, 2019.

Grandin, M., Turc, L., Battarbee, M., Ganse, U., Johlander, A., Pfau-Kempf, Y., Dubart, M., and Palmroth, M.: Hybrid-Vlasov simulation of auroral proton precipitation in the cusps: Comparison of northward and southward interplanetary magnetic field driving, Journal of Space Weather and Space Climate, 10, 51, https://doi.org/10.1051/swsc/2020053, 2020.

Grandin, M., Luttikhuis, T., Battarbee, M., Cozzani, G., Zhou, H., Turc, L., Pfau-Kempf, Y., George, H., Horaites, K., Gordeev, E., Ganse, U., Papadakis, K., Alho, M., Tesema, F., Suni, J., Dubart, M., Tarvus, V., and Palmroth, M.: First 3D hybrid-Vlasov global simulation of auroral proton precipitation and comparison with satellite observations, Journal of Space Weather and Space Climate, 13, 20, https://doi.org/10.1051/swsc/2023017, 2023.

Hardy, D. A., Holeman, E. G., Burke, W. J., Gentile, L. C., and Bounar, K. H.: Probability distributions of electron precipitation at high magnetic latitudes, Journal of Geophysical Research (Space Physics), 113, A06 305, https://doi.org/10.1029/2007JA012746, 2008.

Hendrickx, K., Megner, L., Marsh, D. R., and Smith-JohnsenSm, C.: Production and transport mechanisms of NO in the polar upper mesosphere and lower thermosphere in observations and models, Atmos. Chem. Phys., 18, 9075–9089, https://doi.org/10.5194/acp-18-9075-2018, 2018.

Horaites, K., Rintamäki, E., Zaitsev, I., Turc, L., Grandin, M., Cozzani, G., Zhou, H., Alho, M., Suni, J., Kebede, F., Gordeev, E., George, H., Battarbee, M., Bussov, M., Dubart, M., Ganse, U., Papadakis, K., Pfau-Kempf, Y., Tarvus, V., and Palmroth, M.: Magnetospheric Response to a Pressure Pulse in a Three-Dimensional Hybrid-Vlasov Simulation, Journal of Geophysical Research (Space Physics), 128, e2023JA031 374, https://doi.org/10.1029/2023JA031374, 2023.

Häkkilä, T.: hakkila/waccm_iprmlt: IPRMLT, https://doi.org/10.5281/zenodo.11397846, 2024.

Häkkilä, T. and Szelag, M.: Data for the manuscript "Atmospheric Nitrogen Oxide response to electron forcing from a 6D magnetospheric hybrid-kinetic simulation" by T. Häkkilä et. al., https://doi.org/10.57707/FMI-B2SHARE.B8331F7D0DA04DDCA3FD8DFA9B204F93E, 2024.

Kotipalo, L., Battarbee, M., Pfau-Kempf, Y., and Palmroth, M.: Physics-motivated Cell-octree Adaptive Mesh Refinement in the Vlasiator 5.3 Global Hybrid-Vlasov Code, EGUsphere, 2024, 1–24, https://doi.org/10.5194/egusphere-2024-301, 2024.

Manney, G. L., Krüger, K., Pawson, S., Minschwaner, K., Schwartz, M. J., Daffer, W. H., Livesey, N. J., Mlynczak, M. G., Remsberg, E. E., Russell, J. M., and Waters, J. W.: The evolution of the stratopause during the 2006 major warming: Satellite data and assimilated meteorological analyses, J. Geophys. Res., 113, D11 115, https://doi.org/10.1029/2007JD009097, 2008.

Marsh, D. R., Solomon, S. C., and Reynolds, A. E.: Empirical model of nitric oxide in the lower thermosphere, J. Geophys. Res. (Space Phys.), 109, A07301, https://doi.org/10.1029/2003JA010199, 2004.

Marsh, D. R., Garcia, R. R., Kinnison, D. E., Boville, B. A., Sassi, F., Solomon, S. C., and Matthes, K.: Modeling the whole atmosphere response to solar cycle changes in radiative and geomagnetic forcing, J. Geophys. Res. (Atmos.), 112, D23 306, https://doi.org/10.1029/2006JD008306, 2007.

Marsh, D. R., Mills, M., Kinnison, D., Lamarque, J.-F., Calvo, N., and Polvani, L.: Climate change from 1850 to 2005 simulated in CESM1(WACCM), J. Climate, 26, 7372–7391, https://doi.org/10.1175/JCLI-D-12-00558.1, 2013.

Matthes, K., Funke, B., Andersson, M. E., Barnard, L., Beer, J., Charbonneau, P., Clilverd, M. A., Dudok de Wit, T., Haberreiter, M., Hendry, A., Jackman, C. H., Kretschmar, M., Kruschke, T., Kunze, M., Langematz, U., Marsh, D. R., Maycock, A., Misios, S., Rodger, C. J.,

Scaife, A. A., Seppälä, A., Shangguan, M., Sinnhuber, M., Tourpali, K., Usoskin, I., van de Kamp, M., Verronen, P. T., and Versick, S.: Solar Forcing for CMIP6, Geosci. Model Dev., 10, 2247–2302, https://doi.org/10.5194/gmd-10-2247-2017, 2017.

520 Meraner, K. and Schmidt, H.: Transport of nitrogen oxides through the winter mesopause in HAMMONIA, J. Geophys. Res., 121, 2556–2570, https://doi.org/10.1002/2015JD024136, 2016.

Mlynczak, M. G., Martin-Torres, F. J., Crowley, G., Kratz, D. P., Funke, B., Lu, G., Lopez-Puertas, M., Russell, J. M., Kozyra, J., Mertens, C., Sharma, R., Gordley, L., Picard, R., Winick, J., and Paxton, L.: Energy transport in the thermosphere during the solar storms of April 2002, J. Geophys. Res., 110, A12S25, https://doi.org/10.1029/2005JA011141, 2005.

525 Molod, A., Takacs, L., Suarez, M., and Bacmeister, J.: Development of the GEOS-5 atmospheric general circulation model: Evolution from MERRA to MERRA2, Geosci. Model Dev., 8, 1339–1356, https://doi.org/10.5194/gmd-8-1339-2015, 2015.

Palmroth, M., Janhunen, P., Germany, G., Lummerzheim, D., Liou, K., Baker, D. N., Barth, C., Weatherwax, A. T., and Watermann, J.: Precipitation and total power consumption in the ionosphere: Global MHD simulation results compared with Polar and SNOE observations, Annales Geophysicae, 24, 861–872, https://doi.org/10.5194/angeo-24-861-2006, 2006.

530 Palmroth, M., Hoilijoki, S., Juusola, L., Pulkkinen, T. I., Hietala, H., Pfau-Kempf, Y., Ganse, U., von Alfthan, S., Vainio, R., and Hesse, M.: Tail reconnection in the global magnetospheric context: Vlasiator first results, Annales Geophysicae, 35, 1269–1274, https://doi.org/10.5194/angeo-35-1269-2017, 2017.

Palmroth, M., Ganse, U., Pfau-Kempf, Y., Battarbee, M., Turc, L., Brito, T., Grandin, M., Hoilijoki, S., Sandroos, A., and von Alfthan, S.: Vlasov methods in space physics and astrophysics, Living Reviews in Computational Astrophysics, 4, 1, https://doi.org/10.1007/s41115-535 018-0003-2, 2018.

Palmroth, M., Grandin, M., Sarris, T., Doornbos, E., Tourgaidis, S., Aikio, A., Buchert, S., Clilverd, M. A., Dandouras, I., Heelis, R., Hoffmann, A., Ivchenko, N., Kervalishvili, G., Knudsen, D. J., Kotova, A., Liu, H.-L., Malaspina, D. M., March, G., Marchaudon, A., Marghitu, O., Matsuo, T., Miloch, W. J., Moretto-Jørgensen, T., Mpaloukidis, D., Olsen, N., Papadakis, K., Pfaff, R., Pirnaris, P., Siemes, C., Stolle, C., Suni, J., van den IJssel, J., Verronen, P. T., Visser, P., and Yamauchi, M.: Lower-thermosphere–ionosphere (LTI) quantities: 540 current status of measuring techniques and models, Annales Geophysicae, 39, 189–237, https://doi.org/10.5194/angeo-39-189-2021, 2021.

Palmroth, M., Pulkkinen, T. I., Ganse, U., Pfau-Kempf, Y., Koskela, T., Zaitsev, I., Alho, M., Cozzani, G., Turc, L., Battarbee, M., Dubart, M., George, H., Gordeev, E., Grandin, M., Horaites, K., Osmane, A., Papadakis, K., Suni, J., Tarvus, V., Zhou, H., and Nakamura, R.: Magnetotail plasma eruptions driven by magnetic reconnection and kinetic instabilities, Nature Geoscience, 16, 570–576, https://doi.org/10.1038/s41561-023-01206-2, 2023.

545 Partamies, N., Juusola, L., Tanskanen, E., and Kauristie, K.: Statistical properties of substorms during different storm and solar cycle phases, Annales Geophysicae, 31, 349–358, https://doi.org/10.5194/angeo-31-349-2013, 2013.

Pfau-Kempf, Y., von Alfthan, S., Ganse, U., Sandroos, A., Battarbee, M., Koskela, T., Otto, Ilja, Papadakis, K., Kotipalo, L., Zhou, H., Grandin, M., Pokhotelov, D., and Alho, M.: fmihpc/vlasiator: eVlasiator 6D pre-release, https://doi.org/10.5281/zenodo.6642177, 2022.

Pfau-Kempf, Y., von Alfthan, S., Ganse, U., Battarbee, M., Kotipalo, L., Koskela, T., Ilja, Sandroos, A., Papadakis, K., 550 Alho, M., Zhou, H., Palmu, M., Grandin, M., Suni, J., Pokhotelov, D., and kostahoraites: fmihpc/vlasiator: Vlasiator 5.3, https://doi.org/10.5281/zenodo.10600112, 2024.

Picone, J. M., Hedin, A. E., Drob, D. P., and Aikin, A. C.: NRLMSISE-00 empirical model of the atmosphere: Statistical comparisons and scientific issues, J. Geophys. Res., 107, 1468, https://doi.org/10.1029/2002JA009430, 2002.

Randall, C. E., Harvey, V. L., Siskind, D. E., France, J., Bernath, P. F., Boone, C. D., and Walker, K. A.: NO_x descent in the Arctic middle 555 atmosphere in early 2009, Geophys. Res. Lett., 36, L18 811, https://doi.org/10.1029/2009GL039706, 2009.

Randall, C. E., Harvey, V. L., Holt, L. A., Marsh, D. R., Kinnison, D., Funke, B., and Bernath, P. F.: Simulation of energetic particle precipitation effects during the 2003–2004 Arctic winter, J. Geophys. Res. (Space Phys.), 120, 5035–5048, https://doi.org/10.1002/2015JA021196, 2015.

Redmon, R. J., Denig, W. F., Kilcommons, L. M., and Knipp, D. J.: New DMSP database of precipitating auroral electrons and ions, Journal of Geophysical Research (Space Physics), 122, 9056–9067, https://doi.org/10.1002/2016JA023339, 2017.

Roble, P. B. and Ridley, E. C.: An auroral model for the NCAR thermospheric general circulation model (TGCM), Ann. Geophys., 5A(6), 369–382, 1987.

Sarris, T., Palmroth, M., Aikio, A., Buchert, S. C., Clemmons, J., Clilverd, M., Dandouras, I., Doornbos, E., Goodwin, L. V., Grandin, M., Heelis, R., Ivchenko, N., Moretto-Jørgensen, T., Kervalishvili, G., Knudsen, D., Liu, H.-L., Lu, G., Malaspina, D. M., Marghitu, O., Maute, A., Miloch, W. J., Olsen, N., Pfaff, R., Stolle, C., Talaat, E., Thayer, J., Tourgaidis, S., Verronen, P. T., and Yamauchi, M.: Plasma-Neutral Interactions in the Lower Thermosphere-Ionosphere: The need for in situ measurements to address focused questions, Frontiers in Astronomy and Space Sciences, 9, 435, https://doi.org/10.3389/fspas.2022.1063190, 2023.

Seppälä, A., Clilverd, M. A., Beharrell, M. J., Rodger, C. J., Verronen, P. T., Andersson, M. E., and Newnham, D. A.: Substorm-induced energetic electron precipitation: Impact on atmospheric chemistry, Geophys. Res. Lett., 42, 8172–8176, https://doi.org/10.1002/2015GL065523, 2015.

Sinnhuber, M., Kazeminejad, S., and Wissing, J. M.: Interannual variation of NO_x from the lower thermosphere to the upper stratosphere in the years 1991–2005, J. Geophys. Res., 116, A02 312, https://doi.org/10.1029/2010JA015825, 2011.

Sinnhuber, M., Tyssøy, H. N., Asikainen, T., Bender, S., Funke, B., Hendrickx, K., Pettit, J., Reddmann, T., Rozanov, E., Schmidt, H., Smith-Johnsen, C., Sukhodolov, T., Szeląg, M. E., van de Kamp, M., Verronen, P. T., Wissing, J. M., and Yakovchuk, O.: Heppa III intercomparison experiment on medium-energy electrons, part II: Model-measurement intercomparison of nitric oxide (NO) during a geomagnetic storm in April 2010, J. Geophys. Res. (Space Phys.), 127, e2021JA029 466, https://doi.org/<10.1029/2021JA029466, 2021.

Smith-Johnsen, C., Marsh, D. R., Smith, A. K., Tyssøy, H. N., and Maliniemi, V.: Mesospheric nitric oxide transport in WACCM, J. Geophys. Res. (Space Phys.), 127, e2021JA029 998, https://doi.org/10.1029/2021JA029998, 2022.

Szeląg, M. E., Marsh, D. R., Verronen, P. T., Seppälä, A., and Kalakoski, N.: Ozone impact from solar energetic particles cools the polar stratosphere, Nature Commun., 13, 6883, https://doi.org/10.1038/s41467-022-34666-y, 2022.

Tian, S.: The geopack and Tsyganenko models in Python [Software], v1.0.10, Available from https://pypi.org/project/geopack/, 2023.

Tsyganenko, N. A.: A model of the near magnetosphere with a dawn-dusk asymmetry 1. Mathematical structure, Journal of Geophysical Research (Space Physics), 107, 1179, https://doi.org/10.1029/2001JA000219, 2002a.

Tsyganenko, N. A.: A model of the near magnetosphere with a dawn-dusk asymmetry 2. Parameterization and fitting to observations, Journal of Geophysical Research (Space Physics), 107, 1176, https://doi.org/10.1029/2001JA000220, 2002b.

Turunen, E., Kero, A., Verronen, P. T., Miyoshi, Y., Oyama, S., and Saito, S.: Mesospheric ozone destruction by high-energy electron precipitation associated with pulsating aurora, J. Geophys. Res. (Atmos.), 121, 11 852–11 861, https://doi.org/10.1002/2016JD025015, 2016.

van de Kamp, M., Seppälä, A., Clilverd, M. A., Rodger, C. J., Verronen, P. T., and Whittaker, I. C.: A model providing long-term datasets of energetic electron precipitation during geomagnetic storms, J. Geophys. Res. (Atmos.), 121, 12 520–12 540, https://doi.org/10.1002/2015JD024212, 2016.

Verronen, P. T. and Rodger, C. J.: Atmospheric ionization by energetic particle precipitation, chap. 4.5, pp. 261–266, Earth's climate response to a changing Sun, edited by T. Dudok de Wit et al., EDP Sciences (www.edpsciences.org), France, ISBN 978-2-7598-1733-7, 2015.

Verronen, P. T., Andersson, M. E., Marsh, D. R., Kovács, T., and Plane, J. M. C.: WACCM-D – Whole Atmosphere Community Climate
595   Model with D-region ion chemistry, J. Adv. Model. Earth Syst., 8, 954–975, https://doi.org/10.1002/2015MS000592, 2016.

von Alfthan, S., Pokhotelov, D., Kempf, Y., Hoilijoki, S., Honkonen, I., Sandroos, A., and Palmroth, M.: Vlasiator: First global hybrid-
Vlasov simulations of Earth's foreshock and magnetosheath, Journal of Atmospheric and Solar-Terrestrial Physics, 120, 24–35,
https://doi.org/https://doi.org/10.1016/j.jastp.2014.08.012, 2014.